Case Studies in Construction Materials 23 (2025) e05192

Contents lists available at ScienceDirect

Case Studies in Construction Materials

journal homepage: www.elsevier.com/locate/cscm

Experimental study on buildability of 3D-printed cement-based structures using aluminium sulphate

Oluwatimilehin Disu *, Sikiru O. Ismail *, Luke Wood, Andreas Chrysanthou, Antonios Kanellopoulos

Centre for Engineering Research, School of Physics, Engineering and Computer Science, University of Hertfordshire, Hatfield, Hertfordshire AL10 9AB, United Kingdom

ARTICLE INFO

Keywords:
3D printing of cement-based materials
Accelerator
Buildability
Structural stability
Failure mode

ABSTRACT

Recent advancements in Additive Manufacturing (AM), specifically in 3D printing of cement-based materials, have highlighted the necessity for enhancing buildability through optimising material properties and printing parameters. This study explored the effects of printing speed, layer height and the use of aluminium sulphate ($Al_2(SO_4)_3$) as an accelerator on the buildability of small-scale cement-based structures. Utilising mastercrete cement, fly ash and ground granulated blast-furnace slag (GGBS), the influence of the above variables on the structural integrity of 3D-printed layers was examined. Experimental results indicated that increasing the aluminium sulphate concentration to a 45% concentration improved buildability. This optimal concentration supported samples of 14 layers to be built, demonstrating enhanced stiffness and load-bearing capacity. The optimal printing speed of 20 mm/s achieved a balance between material deposition and setting time, facilitating the printing of 10 stable layers without accelerator. Conversely, increasing the printing speed resulted in a reduced buildability, due to poor adhesion between layers. Layer height analysis revealed that a layer height of 10 mm was most effective, ensuring proper interlayer adhesion and structural stability. These parameters significantly enhanced the buildability and collectively supported the structural integrity and feasibility of cement-based 3D printing for construction applications.

1. Introduction

Additive manufacturing (AM) of concrete, commonly referred to as concrete 3D printing, is a fast-evolving construction technology that enables the creation of complex concrete structures without the need for traditional formwork, using a layer-by-layer deposition process [1–4]. In recent years, the building and construction industry has experienced rapid interest in the development of 3D printing from the conception and formation of printable materials to the design and implementation of new printable systems and commercialisation [5–10]. A major issue involved in the adoption of AM in the construction industry is the size constraint of printed structures [11–14]. Recent research has developed new materials and methods to conduct 3D printing of cement-based structures. The main materials used for extrusion-based AM in construction are cement-based composites. These composites consist of cement, admixtures, fine aggregates, secondary cementitious materials, air and water, among other materials, with the capability of nozzle extrusion [15]. Since concrete is the most widely used construction material globally, its environmental impact has drawn increasing attention.

* Corresponding authors.
E-mail addresses: o.disu@herts.ac.uk (O. Disu), s.ismail3@herts.ac.uk (S.O. Ismail).

https://doi.org/10.1016/j.cscm.2025.e05192
Received 1 March 2025; Received in revised form 7 August 2025; Accepted 17 August 2025
Available online 18 August 2025

Despite its many advantages over other materials, conventional concrete relies heavily on cement, whose production is a major contributor to greenhouse gas emissions. Cement manufacturing accounts for approximately 8% of global CO_2 emissions and generated nearly 4.1 gigatonnes of CO_2 in 2017 alone. Therefore, developing sustainable and printable cement-based composites for AM presents a dual opportunity to innovate in construction methods while addressing critical environmental challenges [16–18].

Over the years, many researchers have studied and investigated the application of AM of concrete to the building and construction industry. One major hurdle to overcome is the issue of weak interlayer bonding between deposited layers, the effect of the time gap between successful deposition of material, which is highly dependent on the fresh properties of concrete, such as rheology and printing parameters, including printing speed and nozzle height [19–26], and other factors that affect the buildability of 3D-printed structures. One factor that influences buildability is the yield strength of the printable concrete. An increase in yield strength enhances buildability [27,28]. Achieving optimal 3D concrete printing requires materials with key rheological properties, specifically pumpability for smooth transport to the print head, and extrudability for consistent and continuous extrusion [29]. Buildability is also impacted by ability of a layer to recover its original viscosity and yield stress before the next layer is deposited. As yield strength increases with elapsed time [30], buildability is affected by the time gaps between printing layers. A study on interlayer bond strength revealed that the bond strength is highly dependent on the open time or the change in workability over time [27,31]. Panda et al. [32] investigated the impact of varying nozzle speeds on the properties of fresh concrete used in 3D printing of cement-based materials and showed that an optimal printing speed supported a consistent layer bead width throughout the process. However, it was also observed that the bonding strength of the printed layers slightly decreased with increasing nozzle speed. Similarly, Kruger et al. [33] developed a design model for 3D concrete printing that predicted the optimal printing speed to prevent structural failure under specific conditions.

Furthermore, the rheological properties play a crucial role in the 3D printing of cement-based materials [34–37]. It changes continuously, due to the ongoing hydration process. Although, fresh concrete can be easily extruded, its workability or open time for printing is shorter than in conventional applications [38–42]. As viscosity increases over time, workability decreases until the material becomes too stiff to be extruded. This stiffening of the cementitious matrix, while complicating the printing process, also enhances the mechanical strength of the initial layers, allowing them to better support subsequent layers. Therefore, rheological measurements are essential for determining the casting properties of fresh concrete, including workability, flowability and especially printability [38, 43–46]. Other studies focused on the addition of alkali-free setting accelerator at the print head [43,47]. A dosage of 2.5% accelerator by weight of the binder increased the Bingham yield strength by six-fold when compared with the reference paste. This effect was attributed to the fact that the alkali-free accelerator (primarily composed of aluminium sulphate), accelerated the crystallisation of ettringite [43]. Ettringite is a crystalline compound formed when the accelerating admixture is sprayed onto the surface of the 3D-printed cement-based structure [43,48]. Consequently, the use of accelerators impacted the microstructure, thereby influencing the rheology, as discussed by numerous researchers [43–45,49,50]. Therefore, the addition of an accelerator directly affects the rheological behaviour, setting and hardening of the mix, ultimately impacting buildability.

Recent research has also highlighted the role of creep deformation and thixotropic recovery in influencing buildability. Creep, defined as the time-dependent deformation of fresh material under its own weight, has been shown to contribute to layer instability and collapse if the material lacks sufficient static yield stress [51]. Conversely, thixotropy, the ability of the material to rebuild its internal structure after shear, has been identified as a key mechanism enabling stable multi-layer deposition [52]. These rheological behaviours are increasingly recognised as critical factors in achieving printability and structural stability in 3D-printed cement-based materials.

Besides, role of on-demand spraying of aluminium sulphate on the buildability of 3D-printed cement-based structures cannot be underestimated. The cement-based 3D printing industry requires a method to enhance buildability post-printing to mitigate the risk of early-age structural failure. To address this, a novel method of applying an accelerator has been developed, specifically aimed at improving buildability after the printing process. A study conducted by Bhattacherjee and Santhanam [43] concluded that higher dosages of accelerators significantly reduced the setting time of cement-based materials. An 8% accelerator reduced the setting time to 4.5 min, while a 2% dosage decreased it from 3 h 15 min to 2 h 30 min. Penetration resistance tests with 1, 2 and 3% accelerator dosages showed that the initial setting time was corresponding to 3.43 N/mm^2 and the final setting time to 26.97 N/mm^2. A 3% accelerator reduced the initial setting time to 3.5 h and the final setting time to 6.2 h, with build-up starting after 2 h. The 1 and 2% dosages also reduced setting times by about 1.5 and 1.0 h, respectively. Higher dosages accelerated ettringite formation, promoting faster build-up. In another study, Bhattacherjee and Santhanam [53] observed that when aluminium sulphate was used as an accelerating agent and sprayed on-demand on the surface of 3D-printed cement-based structures, it increased flocculation and the rate of hydration, enhancing the yield strength of the outer layer. This strengthened outer layer acted as a sacrificial barrier, preventing plastic deformation under subsequent loads [43]. Furthermore, when the accelerating admixture was sprayed at a distance of 50 mm from the surface, X-ray diffraction tests showed ettringite formation up to a depth of 5–7 mm from the surface, with no ettringite found beyond this depth. Ettringite contributed to the early strength development and stability of the surface layer, but it was not detected beyond this depth, indicating its localised effect.

To advance knowledge on 3D printing of cement-based structures, there is a necessity to study the effects of important parameters on buildability of printed structures. While previous studies, including the work of Bhattacherjee and Santhanam [53], have demonstrated that surface application of aluminium sulphate can improve buildability in 3D-printed cementitious materials, their approach relied on manual spraying and examined accelerator dosage in isolation. In contrast, the present study introduced a robot-controlled, layer-by-layer surface misting system that allowed for precise and consistent application of accelerator during the printing process. Furthermore, this research presented a robot-controlled, layer-by-layer surface misting system that enables precise accelerator application during printing. It investigated the combined influence of printing speed, layer height and accelerator dosage on buildability, providing a reproducible and scalable process model suitable for industrial 3D printing applications.

Therefore, this study focused on the development of robot-assisted 3D printing of small-scale cement-based structures by understanding the effect of printing speed, layer height and aluminium sulphate used as an accelerator on the extrudability and mainly buildability of the structures. The research further investigated the optimal combination of material properties and printing parameters for enhanced structural integrity and the feasibility of cement-based 3D printing for construction applications.

2. Materials and methods

2.1. Materials

2.1.1. Raw materials

This study utilised Portland-limestone mastercrete cement (CEM II/A-L) [54] produced by the Tarmac company which conforms to the BS EN 197–1 CEM II/A-L [54]. The properties included, but are not limited to, lower water demand, enhanced resistance to thaw attack and freeze, and reduced likelihood of water segregation and bleeding. Fly ash 450-N that was produced according to the BS EN 450–1 standard was used as an additive to enhance the mechanical properties of the 3D-printed structures [55]. The fly ash conformed to the normal fineness (N) Category of BS EN 450–1:2005 and met the requirements for Loss on Ignition Category B (2–7%). Although the maximum permitted residue on a 45 μ sieve was 40%, test results for the product typically fell well within the limit. The powder had a bulk density ranged from 800 to 1000 kg/m^3. Another additive used was Ground Granulated Blast-furnace Slag (GGBS), according to the BS EN 15167–1:2006 [55]. Building sand was used as a fine aggregate with a maximum particle size of 1 mm. An optimum water/binder ratio of 0.45 was used to ensure workability.

2.1.2. Chemical accelerator

The chemical accelerator was aluminium sulphate, a chemical compound with the formula $Al_2(SO_4)_3$. Aluminium sulphate acted as an accelerator during the 3D printing process, promoting faster setting times [43,53]. The specific product used was aluminium sulphate octa-decahydrate, which was available in a highly pure form.

2.1.3. Mixture design and protocol

Table 1 presents the mixture design used to conduct this research. The binder-to-sand ratio was 1.5:2. Additives, such as fly ash and GGBS were added to the mixture to improve the cement properties. The binder mixture consisted of 20, 30 and 50% of GGBS, fly ash and cement, respectively.

The physical properties and chemical composition of the cement-based materials used in this study are presented in Table 1. The materials include sand, cement, Fly Ash, GGBS, and $Al_2(SO_4)_3$, with Fly Ash and GGBS used to partially replace cement on a mass-for-mass basis. For the 3D printing process, sand particles were sieved in batches using a metallic sieve due to the particle size restriction on the mortar pump, which has a maximum tolerance of 1.5 mm. Therefore, sieve analysis was conducted. Prior to this, the sand was dried in an oven at 100–120 °C for 48 h to remove any moisture content. This drying process was crucial to accurately determine the water/binder ratio because any residual moisture in the sand could have a negative impact on the ratio calculation. This could affect the workability of the mixture. Dry materials (sand, cement, fly ash and GGBS) were weighed and mixed, using a Soroto cement mixer. The mixer was inspected for cleanliness and set up on a stable surface. The mixing sequence included sand, cement, fly ash and GGBS, followed by 5 min of machine mixing, 2 min of manual mixing and another 5 min of machine mixing. Water was added slowly in one-go into the mixer, followed by 4 min of machine mixing and 2 min of manual mixing and a final 4 min of machine mixing, totalling 10 min. The prepared material was then transferred to the cement pump for 3D printing. Using correct personal protective equipment, the mixing process for aluminium sulphate involved measurement of the required amount of aluminium sulphate, mixing it with deionised (DI) water to ensure purity by removing ions, minerals and salts. The aluminium sulphate was thoroughly dissolved in the DI water through manual stirring, followed by a settling period which took between 20 and 30 min to completely dissolve, depending on

Table 1
Mixture design.

Material	Quantity (kg/m^3)	Technical properties	Supplier
Fine building sand	40	$\leq$ 1.0 mm Chlorides $\leq$ 0.01% Acid soluble sulphates $\leq$ 0.8 Total Sulphur $\leq$ 1% Drying shrinkage $<$ 0.01%	Travis Perkins
Mastercrete cement	20	Conforming to BS EN 197–1 CEM II/A-L	Tarmac
Fly ash	12	Conforming to BS EN 450–1 Finess category N LOI Category B Loss of ignition $<$ 7% Density 800–1000 kg/m^3 Silica 50%, Alumina 26%	Conserv
Ground Granulated Blast-furnace Slag (GGBS)	8	Conforming to BS EN 15167–1:2006	Conserv
Water	45% of binder weight.		————
$Al_2(SO_4)_3$	15, 25, 35 and 45%	CAS – 7784–31–8	Fisher Scientific

the concentration.

2.1.4. Cement-based 3D printing robot

The Mitsubishi robot used was a vertical 6-axis multiple-jointed type with an optimised arm length, allowing a wide range of movement for complex assemblies and process operations. It had a maximum load capacity of 3 kg (rated 2 kg) and a maximum reach of 504 mm. The robot featured a compact body and slender arms, covering a large work area and operating in both automatic and manual modes. The robot design addressed corrosion resistance, achieved using stainless steel and special coatings. The robot uses a standalone controller, the CR750D, as shown in Fig. 1. The controller featured a control nucleus for constructing cells (Mitsubishi Industrial Robot Manual, 2022) and supported system development for various applications.

2.1.5. Pumping system

The Compact Pro 10 mortar pump used in this research featured a progressive cavity pumping system with a metal rotor and elastomer stator, ensuring efficient, minimal pulse and low shear flow. Its design included large-diameter wheels and shaft-type handles for enhanced portability. The pump allowed for adjustable speed and pressure, and the rotor was reversible hence it offered high flow accuracy and reliability. The purpose of this pump was to convey fresh cement-based materials through a 25 mm diameter pipe to the robot extrusion nozzle. Table 2 presents the technical properties of the cement pump.

2.2. Nozzle design

The nozzle was designed and manufactured in-house at the University of Hertfordshire, UK. Aluminium was selected for the nozzle material because of its lightweight, workable, corrosion-resistant and recyclable properties. The nozzle has an outlet thickness of 4 mm and an inner diameter of 20 mm. A compression mechanism was introduced and added to the robot nozzle to aid extrudability, reducing the inner diameter of the extrusion nozzle from 20 to 15 mm. The inlet pipe was welded at 30° to prevent stress concentration, as reported by Cali [56]. The nozzle has a shorter length of 120 mm to avoid overloading on the robot arm. The inlet pipe had a threaded groove to improve the connection between the cement pipe and the nozzle inlet. Fig. 2 shows the nozzle connected to the robot part.

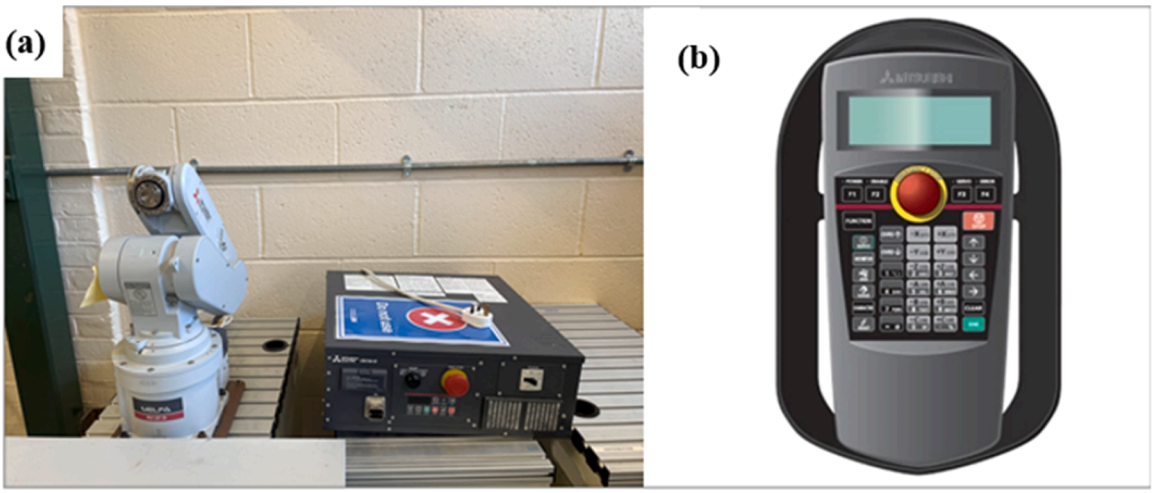

Fig. 1. (a) Mitsubishi 6-axis robot and (b) its pendant.

Table 2
Technical properties of the cement pump used.

Technical properties	Quantity
Product pressure	0–20 bar
Product flow rate	0–8 kg/min
Power supply	110 v/16 A/50 & 60 Hz
Motor power	0.55 kw
Integrated compressor	No
Tank capacity	37 L
Maximum grain size	1.5 mm
Pipe diameter	25. m

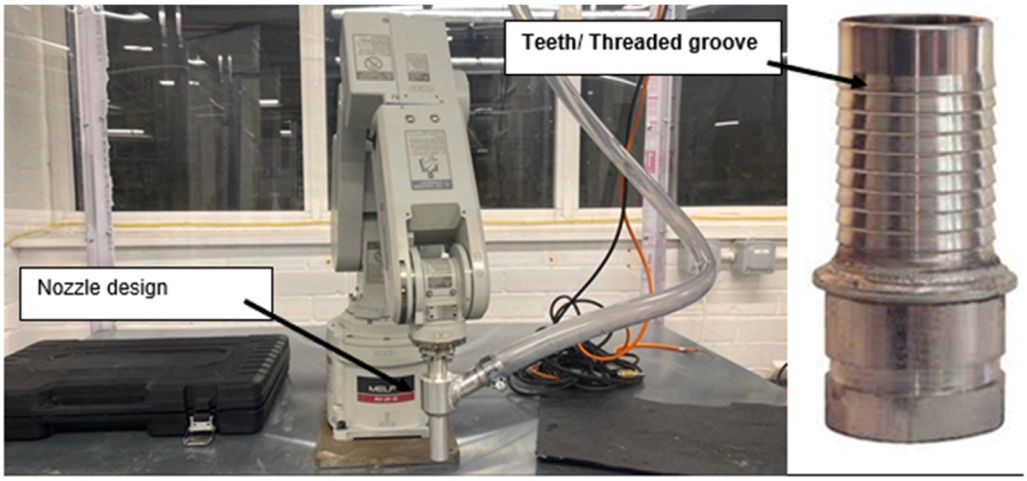

Fig. 2. Nozzle design with threaded groove.

2.3. Experimental methods and procedures

2.3.1. Programming software and path

The software used is the latest version of Mitsubishi RT ToolBox3, which is a next-generation programme creation software, as compared with its predecessor RT Toolbox 2. The software uses the MELFA-BASIC programming language with MELFA-BASIC VI, as used for this research. A rectangular structure was chosen, due to its simple design and wall-like replica. Before 3D printing of a rectangular structure, the speed was defined and coordinates were recorded for six positions: P0 (starting point), P1-P4 (corners) and P5 (material deposition point). The "mov" and "Mvs" commands were used for joint and linear interpolations, respectively. Single or double quotes indicated printing layers. The programme ended with the "End" command. Fig. 3 depicts the path movement of the robot extrusion nozzle.

2.3.2. Printing speeds

This study evaluated four different specimens that were 3D-printed with varying printing speeds. The structures were printed with speeds of 10, 20, 40 and 80 mm/s with a layer height increment of 10 mm. A constant pumping pressure of 2 bar was maintained. The environmental temperature and humidity at the time of printing were 11.5 °C and 73%, respectively. One of the objectives of the experiment was to observe how the different printing speeds would affect the buildability of the 3D-printed small-scale structures, while keeping other parameters constant. The pumping pressure remained constant at 2 bar.

2.3.3. Layer height

Similar to the previous procedure used for printing speed, four different structures were 3D-printed and evaluated based on a difference in the layer height. The structures were printed with a layer height increment of 5 mm, having samples C1, C2, C3 and C4 at 10, 15, 20 and 25 mm, respectively. The layer width and the number of layers printed before structural failure were recorded for each

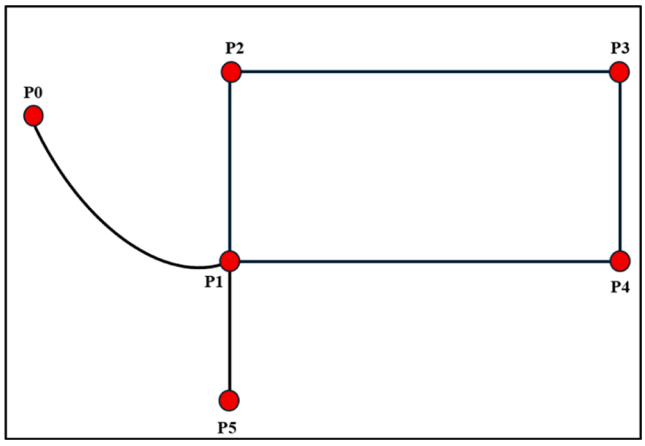

Fig. 3. Robot 3D printing path.

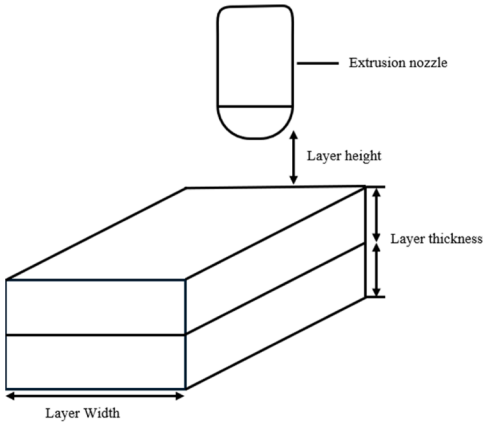

Fig. 4. Schematic diagram, showing layer height, thickness and width in a 3D printing of cement-based material.

sample. Both constant pumping pressure and printing speed of 2 bar and 20 mm/s were maintained, respectively. The environmental temperature and humidity at the time of printing remained 11.5 °C and 73%, respectively. Fig. 4 depicts the schematics of the 3D nozzle and extruded layers

2.3.4. Aluminium sulphate

Buildability was evaluated by the number of deposited layers and the overall layer height. All layers were printed with a consistent time gap of 50 s. One sample, labelled CTRL_ST00, served as the control sample with no aluminium sulphate. The other samples containing accelerator dosages of 10, 15, 25, 35 and 45% were used for the 3D-printed samples AL_ST15, AL_ST25, AL_ST35 and AL_ST45, respectively. The accelerator was pumped through a small peristaltic pump, operating at a maximum flow rate of 600 ML/m. To ensure an even distribution of the accelerator onto each layer, the accelerator nozzle diameter of 6 μm was attached to a robot nozzle, which then sprayed the mixture onto each deposited layer. The diameter of the extrusion nozzle was 15 mm, and the 3D-printed structure measured 440 × 140 mm with a layer width of 40 mm. Continuous printing was conducted until the structure failed to determine the maximum layer height. Environmental factors, such as temperature of 15 °C and humidity of 62%, were closely monitored at the start to the end of 3D printing, providing a comprehensive understanding of the experimental outcomes.

2.4. Experimental methods

2.4.1. Flowability test

The mortar flow table test, according to BS EN 12350–5, was used to assess the workability of four mortar mixtures for 3D printing of cement-based material. Each batch was mixed to achieve different flow characteristics. For each mixture, mortar was placed in a mould on the flow table, compacted to remove air, and the mould was lifted. The table was dropped 15 times, and the spread diameter was measured in two directions, with the average recorded. Each test was repeated three times to ensure consistency, and all equipment was calibrated for accuracy. This standardised method is well-supported in the literature as an effective technique for evaluating printable mortar flowability, as reported by Li et al. [57] and Krishnaraja and Guru [58]. Figs 5(a)-(c) show the progression of the slump test, illustrating the (a) initial state, (b) intermediate deformation and (c) final spread of the mortar sample after mould removal.

Fig. 5. Flow table test.

2.4.2. Penetration resistance

The setting time of the prepared cementitious material was evaluated, using the Vicamatic-2 automatic Vicat apparatus, as shown in Fig. 6. This test aimed to determine the impact of aluminium sulphate surface treatment on the hydration behaviour of the mix design. The paste was prepared according to the specified mix proportions and placed in a standard conical mould, ensuring a flat surface. To simulate on-demand surface treatment, aluminium sulphate at varying concentrations was sprayed onto the paste surface. The mould was then positioned inside the Vicamatic-2 chamber, aligning the sample beneath the Vicat needle. Test parameters were set to a 40-second penetration interval and a maximum penetration depth of 40 mm. The machine automatically performed the penetration tests, recording the depth of each cycle. The initial and final setting times were noted upon completion, and the equipment was thoroughly cleaned.

2.4.3. Extrudability test

To achieve an effective 3D printing system, a flowability and/or extrudability test was conducted. Flowability is the ability of a material to flow smoothly from the mixer to the print nozzle. This property is critical in the evaluation of the flow behaviour of fresh material in the pumping system [59]. Extrudability is the ability of the material to pass through the printing nozzle with ease, a continuous and intact filament. The term extrudable is used when the extruded material retains its shape with no imperfections over a long distance [15]. Fig. 7 shows a well extruded material, confirming effective 3D printing process.

Fig. 6. Penetration resistance test machine.

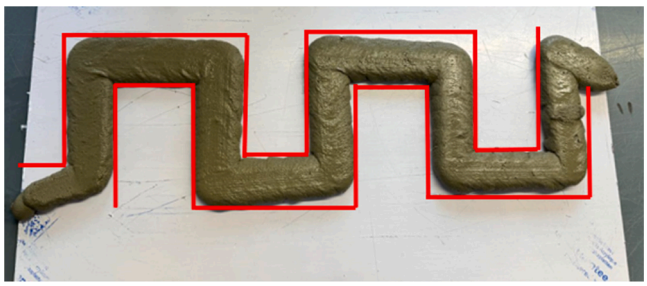

Fig. 7. Extrudability test sample.

2.5. Overall 3D printing process

Precise preparatory steps and equipment are essential to ensure consistent and excellent quality of the cement-based materials used in 3D printing. Figs 8 and 9 depict the flowchart and the overall 3D printing process, respectively.

Moreover, the mortar mixer was used for efficient and precise mixing of the cement-based materials. When the mixing was

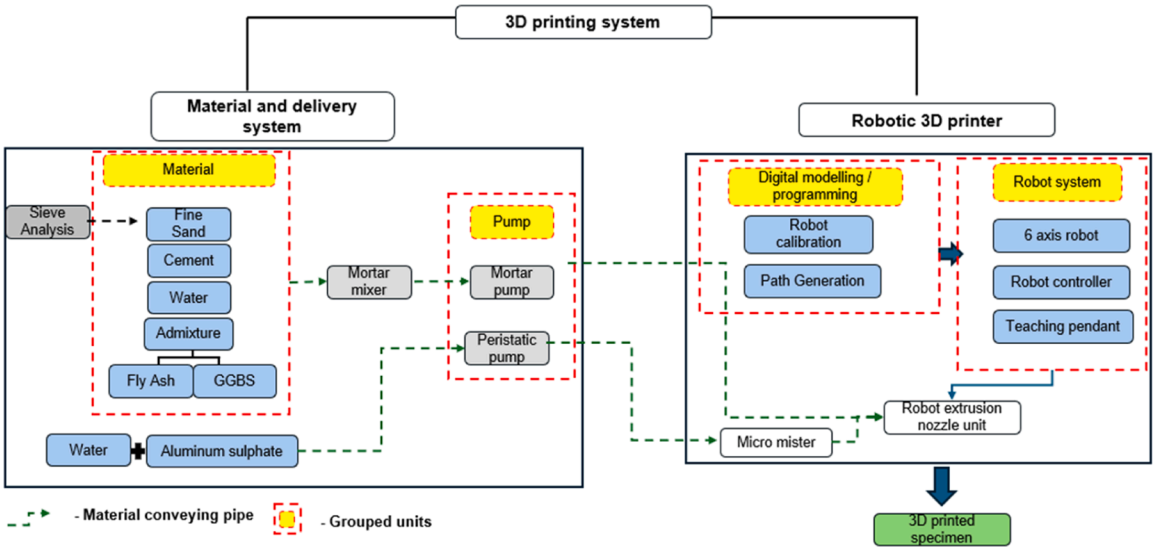

Fig. 8. Flowchart of 3D printing process.

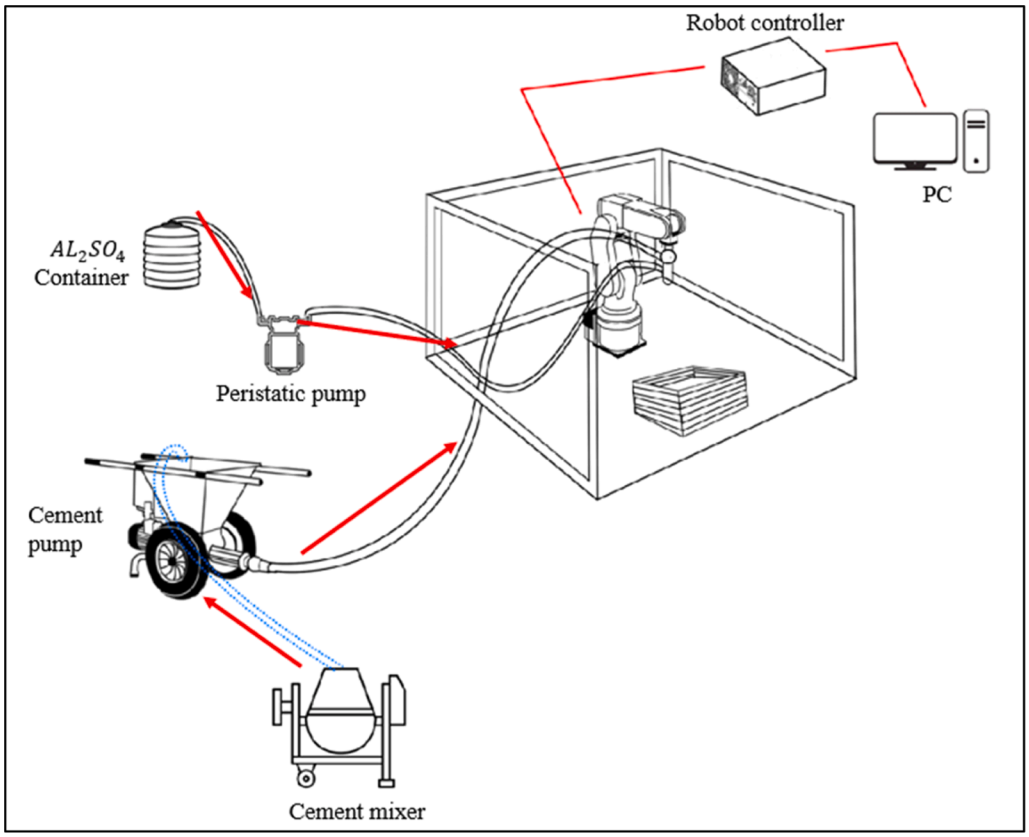

Fig. 9. Overall 3D printing process.

completed, the cement pump was turned on, and the rotor began to rotate. Clean water was used to flush the system down before the prepared cement mixture was fed into a hopper, which connected to the cement pump. The hopper acted as a reservoir, ensuring a continuous flow of material during the printing process. The cement pump pushed the mixture through the material, conveying the pipe to the robot extrusion nozzle. The nozzle was a critical component, as it allowed the flow and deposition of the cement material. Before printing started, the system was allowed to extrude the cement-based material, washing away the water within the system and extracting the air bubbles. This step was crucial to get rid of potential voids, blockages or interruptions during the 3D printing process. The formation of air bubbles is an extremely complex phenomenon influenced by various factors, such as the mixing process, concrete mixture proportioning, characteristics of cement and aggregates, water content and other chemical admixtures [60].

To begin the 3D printing process, a specialised 6-axis robotic system was used to deposit layers of cement-based material layer by layer. A Cartesian coordinate method was used to take the target point, which the robot system followed along the x, y and z axes, allowing the nozzle to move and create the desired structure layer by layer. During this process, a peristatic pump also pumped accelerator from an accelerator storage tank to the micro mister that was attached to the nozzle of the robot. The micro mister was a small device the sprayed accelerator on the just deposited layer in form of mist to avoid overflow of the accelerator. The robot system operated with Cartesian motion to ensure accuracy and precision. The movement of the robot nozzle was precisely controlled by the robotic arm. A high level of precision in depositing material was essential and therefore obtained for accuracy in layer deposition and ensuring the stability of the printed structure. The extrusion process plays a crucial role in 3D printing. The movement of the nozzle was synchronised with the extrusion process to improve the quality of the 3D-printed structure. The quality of the 3D-printed material was highly dependent on the printing speed, pump speed and layer height, among other factors, as subsequently elucidated.

3. Results and discussion

3.1. Flowability

Four mortar mixtures were tested to examine the influence of sand gradation, water-to-binder ratio (W/B) and supplementary cementitious materials (SCMs) on flowability. Workability was assessed using slump and slump-flow tests. As presented in Table 3, the results established distinct patterns, highlighting the role of sand type and binder composition in affecting extrudability and suitability for 3D printing of cement-based material.

The workability of the four mortar mixtures varied significantly, depending on the sand type, sand-to-binder ratio (S/B), water-to-binder ratio (W/B) and the inclusion of supplementary cementitious materials (SCMs).

Mixtures 1 and 2 were prepared with sharp sand and without SCMs, both maintaining a W/B of 0.40. However, Mix 1 had a higher S/B of 4.00, resulting in the lowest workability, with a recorded slump of 1.8 mm and a slump-flow of 118 mm. This outcome can be attributed to the high sand content, which limited paste mobility and contributed to a stiff, unworkable mix. A reduction in S/B to 3.00 in Mix 2 produced a modest improvement in flowability, increasing the slump to 2.7 mm and the slump-flow to 127 mm. These results were consistent with those reported by Papachristoforou et al. [61], it was noted that reducing sand content enhanced the binder-to-aggregate balance, thereby improved flowability.

In contrast, Mixtures 3 and 4 demonstrated substantially higher workability. Both utilised fine sand and incorporated SCMs, specifically fly ash (FA/B = 0.20) and ground granulated blast-furnace slag (GGBS/B = 0.30). Mix 3, with an S/B of 1.33 and W/B of 0.40, achieved a slump of 3.9 mm and a slump-flow of 144 mm, placing it close to the recommended printable range of 145–190 mm, as identified by Wei et al. [62].

Mix 4, which maintained the same binder composition as Mix 3, but increased the W/B to 0.45, exhibited the highest workability, with a slump of 4.5 mm and a slump-flow of 152 mm. The increased water content enhanced mixture fluidity while maintaining sufficient buildability, supporting the recommendations of Le et al. [31] for achieving an optimal balance between extrudability and structural stability in 3D printable mortars. Based on these observations, Mix 4 was selected as the most suitable formulation to conduct further experiments.

3.2. Penetration resistance

Penetration resistance tests were carried out, using the Vicat apparatus to evaluate the influence of aluminium sulphate on the early stage setting behaviour of the mortar mixes. A total of five mixes were examined, including one control sample (CTRL_ST00) without accelerator and four treated samples containing increasing dosages of aluminium sulphate, designated as AL_ST15, AL_ST25, AL_ST35 and AL_ST45. The progression of penetration depth over time for all tested samples is shown in Fig. 10, providing a comparative assessment of how the accelerator dosage affected the setting development.

Table 3
Mix composition and workability performance.

Mix.	Sand type	W/B	S/B	FA/B	GGBS/B	Slump (mm)	Slump-flow (mm)
1	Sharp	0.40	4.00	—	—	1.8	118
2	Sharp	0.40	3.00	—	—	2.7	127
3	Fine	0.40	1.33	0.20	0.30	3.9	144
4	Fine	0.45	1.33	0.20	0.30	4.5	152

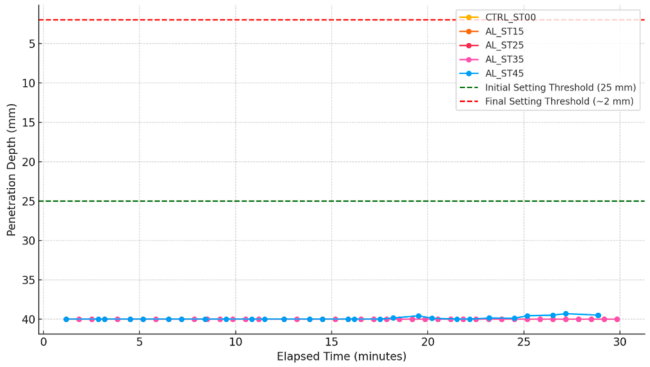

Fig. 10. Penetration resistance *versus* time.

The penetration resistance results for all five mortar mixes are depicted in Fig. 10, showing the progression of penetration depth over time. Across the 30-minute testing period, all mixes maintained consistent penetration depths between 39 and 40 mm, with none of the samples reaching the initial setting threshold of 25 mm or the final setting limit of approximately 2 mm, as specified in BS EN 196–3. These results indicated that no observable setting occurred within the duration of the test for any of the mixes evaluated.

A minor reduction in penetration depth was observed for AL_ST45, the mix containing the highest concentration of aluminium sulphate, where the penetration depth decreased slightly to 39.8 mm after 17 min. Although, this reduction was minimal and remained well above the initial setting threshold. It may suggest the earliest signs of setting development in the sprayed accelerated mix.

It is important to note that the Vicat apparatus applies a localised, point-based load, which may not fully represent the actual conditions in extrusion-based 3D printing of cement-based material. In practical applications, the layer-by-layer deposition process applies distributed surface pressure rather than a single point load. This surface contact pressure can enhance buildability and structural stability even before measurable setting is detected by conventional methods.

This distinction is particularly relevant, because small-scale 3D-printed elements are typically completed in under 30 min, requiring the material to support the load of subsequent layers before reaching conventional setting thresholds. Therefore, while the Vicat test did not indicate significant setting within the observed period, practical buildability may still be achievable through the mechanical effects of surface loading during the printing process. Furthermore, the influence of accelerator dosage on buildability performance under realistic 3D printing conditions has been experimentally studied and reported in the subsequent Section 3.3.

3.3. Effect of aluminium sulphate on buildability of 3D-printed structures

The investigation into the impact of aluminium sulphate as an accelerator on the buildability of 3D-printed cement-based structures focused on understanding how varying concentrations of aluminium sulphate influenced the structural integrity and number of layers that could be successfully printed before collapsing, as shown in Fig. 11. Table 4 presents the effect of aluminium sulphate on the buildability of 3D-printed structures.

Moving forward, the number of layers achieved before structural failure, as depicted in Fig. 12, shows that higher concentrations of accelerator significantly improved the structural integrity and buildability of the 3D-printed layers. Both the CTRL_ST00 sample and the AL_ST15 sample achieved 10 layers before they collapsed. Sample AL_ST25 achieved 11 layers, indicating a slight improvement. The enhancement became more pronounced with sample AL_ST35, which achieved 13 layers, and sample AL_ST45, which achieved 14 layers before failure.

The reduction in height before failure also provided insights into the effects of accelerator dosage on buildability, as shown in Fig. 13. The CTRL_ST00 sample experienced an 8% reduction in height, while both AL_ST15 and AL_ST25 exhibited a 6% reduction. Sample AL_ST35 had a minimal reduction of 2%, and the AL_ST45 sample did not compress before failure. The absence of compression in AL_ST45 suggested that the lower layers became significantly stiffer under the influence of the accelerator concentration, thereby preventing deformation under the weight of subsequent layers. In contrast, the bottom layer of the CTRL_ST00 sample was compressed from 10 to 2 mm, highlighting the benefit of the accelerating admixture to maintain layer integrity.

The results clearly indicated that the optimum concentration for maximum buildability was 45%. At this concentration, the bottom layer of the structure did not compress under the weight of the subsequent layers, unlike the other samples. This phenomenon was significant, as it established that the accelerator/aluminium sulphate not only enhanced the number of layers that could be printed before structural failure, but also improved the stiffness and load-bearing capacity of the 3D-printed layers. Similar findings were reported by Bhattacherjee and Santhanam [43] who printed two large-scale structures, one of which was printed with an accelerator sprayed on the surface. For the first structure, printed in panels, the target height of the lower layer was 15 mm, but the achieved height was only 9 mm, resulting in a compression of 40%. The second structure was printed continuously with simultaneous spraying of the accelerator on the vertical surfaces of the layers, showing higher deformation. The target layer height was 20 mm, and the achieved height was 15 mm, resulting in a compression of 25%. Therefore, this research can conclude that spraying aluminium sulphate on the 3D-printed layer surfaces enhanced their buildability.

Summarily, there was a clear positive correlation between the concentration of aluminium sulphate and the buildability of 3D-

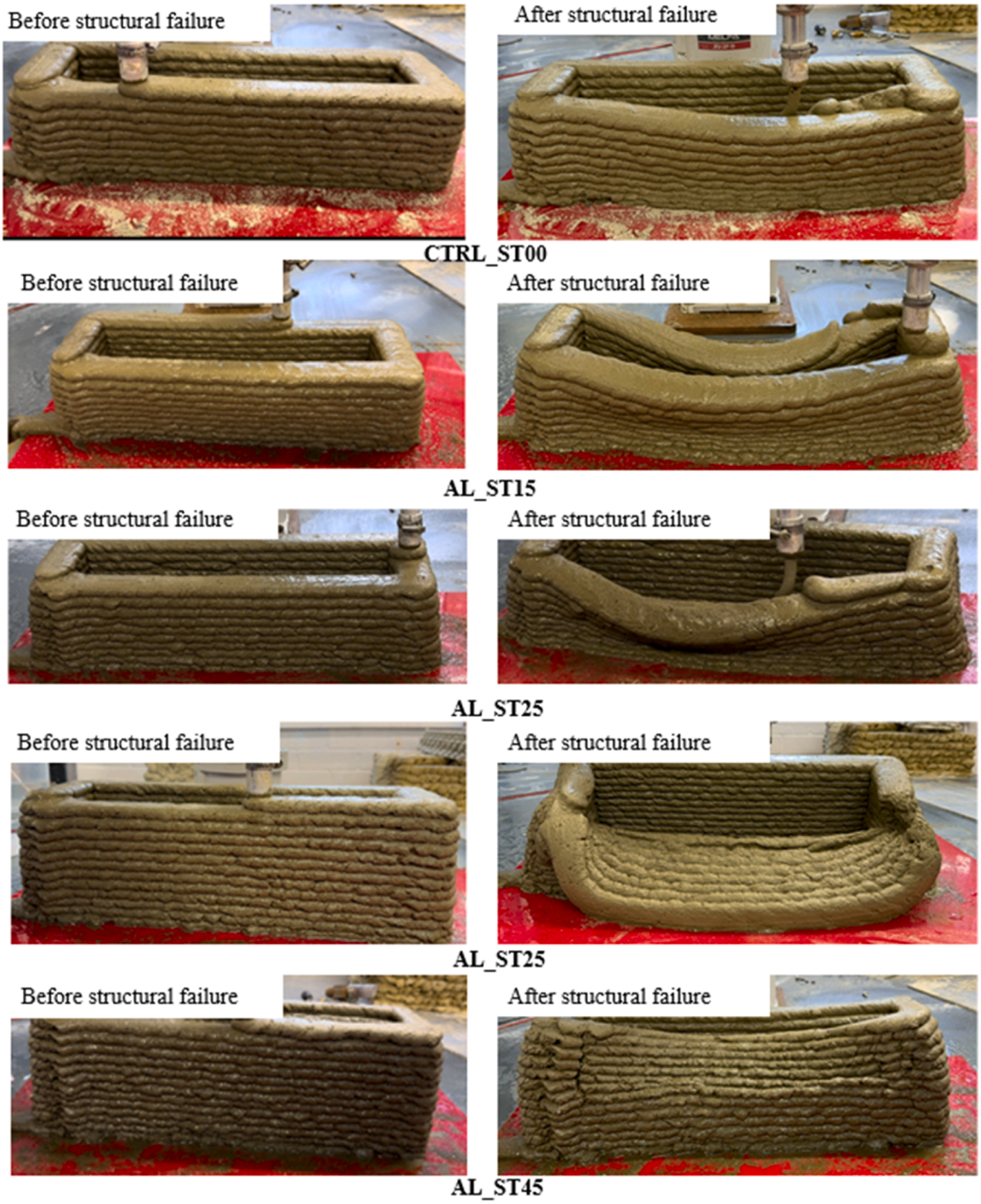

Fig. 11. Buildability test with varying accelerator concentration.

printed structures. The number of 3D-printed layers before structural failure increased or improved from 10 to 14 by increasing the concentration from 0 to 45%. This result was consistent with previous studies [43,53,63,64]; therefore, suggested that accelerators, including aluminium sulphate can enhance the stiffness and load-bearing capacity of 3D-printed layers by accelerating the setting time and improving early-age strength.

In addition, higher aluminium sulphate dosages improved buildability by influencing the time-dependent rheological behaviour of the mix. While the intrinsic rheological properties remain unchanged before hydration, the accelerator enhanced hydration and flocculation, which rapidly increased static yield stress and reduced open time. This accelerated structural build-up allowed layers to

Table 4
Effect of aluminium sulphate on the number of layers.

Parameters	Samples				
	CTRL_ST00	AL_ST15	AL_ST2 5	AL_ST35	AL_ST45
Aluminium sulphate concentration (%)	0	15	25	35	45
No of layers	10	10	11	13	14

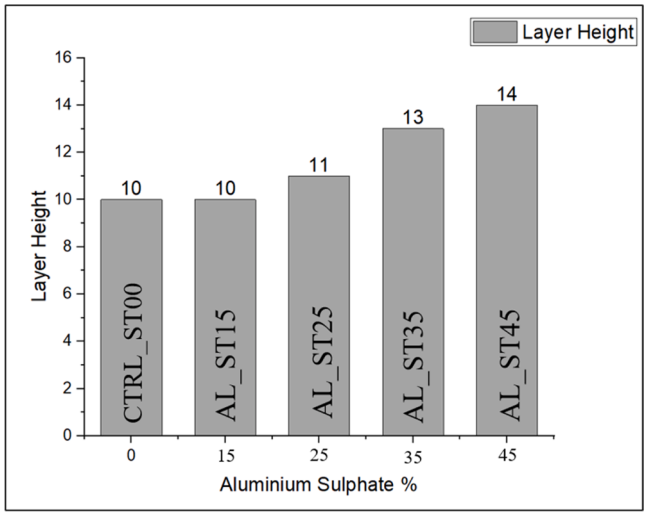

Fig. 12. Influence of accelerator concentration on layer height of the 3D-printed structures.

resist deformation under their own weight and the loading from subsequent layers, as reflected in the improved stability observed at higher dosages. Fig. 14 shows how aluminium sulphate, when applied in controlled amounts, formed a thin, protective layer (pink) on the surface of each 3D-printed layer. This surface layer enhanced buildability by promoting rapid setting, which stabilised the layer and prevented early deformation during the addition of subsequent layers.

Microscopic observations further explained the mechanism by which aluminium sulphate enhanced buildability. The Scanning Electron Microscopy (SEM) image in Fig. 15 shows the microstructure of a sample AL_ST45. Needle-like crystalline formation characteristic of ettringite can be observed densely distributed across the surface. The rapid formation of ettringite, driven by aluminium sulphate hydration reactions, created a rigid interconnected network that filled voids and increased particle interlocking. In addition to ettringite, amorphous gel-like regions of calcium silicate hydrate (C–S–H) were visible, acting as the primary binding phase that consolidated the cement matrix. Plate-like crystalline structures of calcium hydroxide, portlandite (CH) were also observed, contributing to matrix densification.

This combination of early ettringite formation with concurrent CH crystallisation (Fig. 15a) and C–S–H gel development (Fig. 15b) produced a stiffer surface layer capable of resisting deformation under the self-weight of subsequent layers. Similar findings were reported by Bhattacherjee and Santhanam [53], who observed ettringite growth extending up to 5–7 mm. This accelerated microstructural development explained the improved layer stability and reduced compression observed at higher accelerator dosages.

3.3.1. Structural failure

Table 5 presents the different modes of failure from varying the effect of aluminium sulphate on the buildability of 3D-printed structure.

Distinctively, Table 5 provides a comprehensive analysis of the structural behaviours of different 3D-printed cement-based samples, highlighting various failure modes and potential causes. Samples A1, A2, A3, and A4 exhibited signs of elastic buckling, where the structures showed lateral deflections. This mode of failure happens when the lower layers of the samples cannot maintain its geometrical stability [65] under the increasing load from the upper layers, causing it to bend sideways. This suggested that the critical buckling load had been reached. This resulted in significant shape distortions whilst the material remained within its elastic limit. Such deformations occurs because the structure's geometry, particularly its height-to-thickness ratio, makes it more susceptible to buckling under vertical loading. The critical load at which a structure will buckle can be calculated, using Euler's formula (Eq. (1)):

$$P_{cr} = \frac{\pi^2 EI}{(KL)^2} \tag{1}$$

where P_{cr} is the critical buckling load, E is the Young's modulus of the material, I is the moment of inertia of the cross-section, L is the

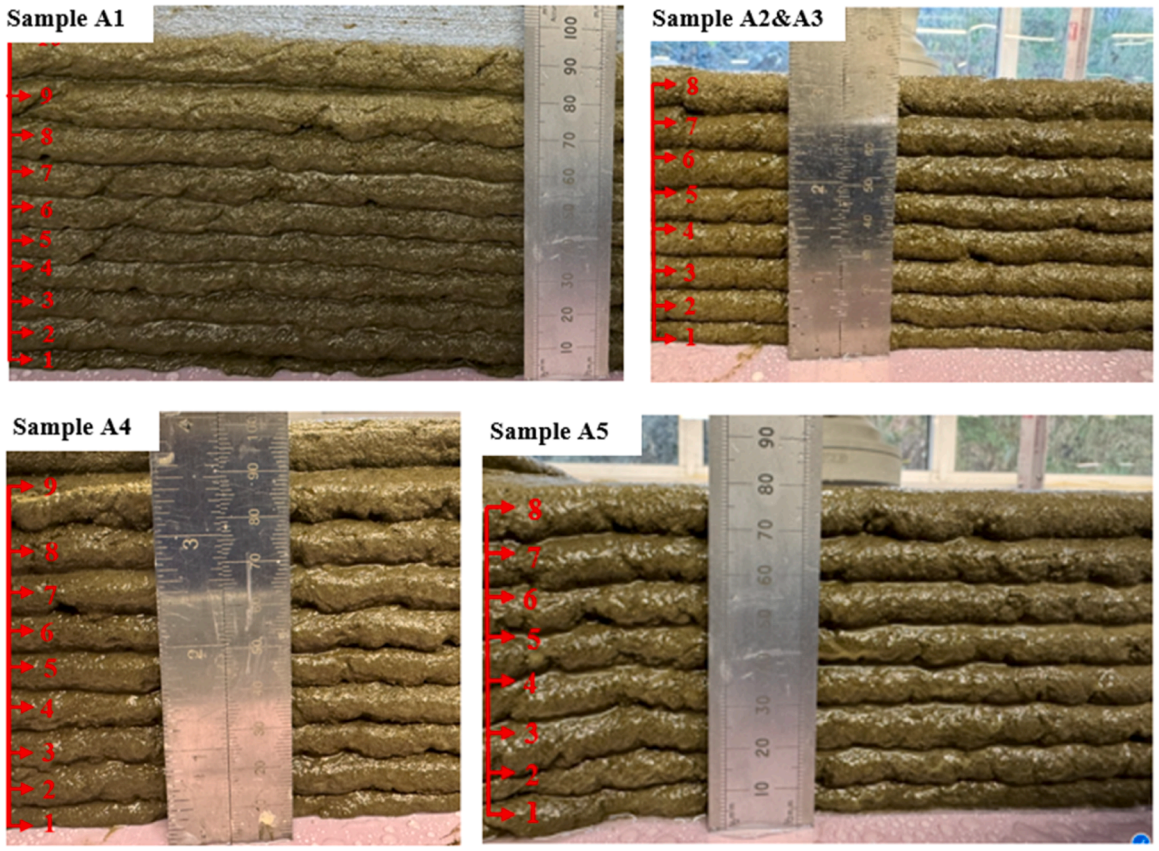

Fig. 13. Reduction in height with varying accelerator concentrations.

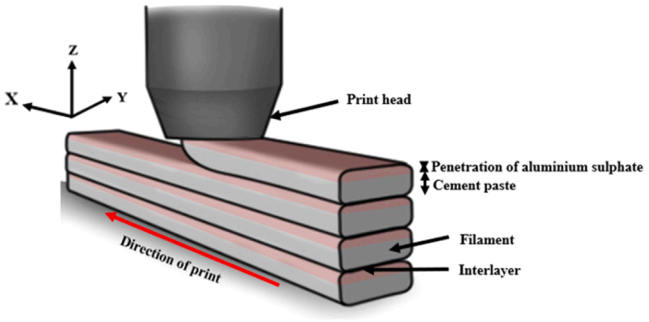

Fig. 14. Penetration of aluminium sulphate.

effective length of the column and K is the effective length factor. The moment of inertia I is directly influenced by the thickness of the. For a rectangular cross-section of width b and thickness t, the moment of inertia is given by Eq. (2):

$$\mathrm{I} = \frac{bt^3}{12} \tag{2}$$

As the thickness t decreases, the moment of inertia I reduces rapidly due to its cubic dependence on t. A lower moment of inertia results in a lower critical buckling load P_{cr}. On the other hand, the height L appears in the denominator of Euler's formula squared. As the height L increases, the critical buckling load decreases significantly. This indicates that tall and slender structures are more likely to buckle under a smaller compressive load compared to shorter, thicker structures with the same material properties.

The susceptibility of a structure to buckling is often quantified using the slenderness ratio (Eq. (3)), defined as the ratio of height, l to thickness, t:

$$\gamma = l/t \tag{3}$$

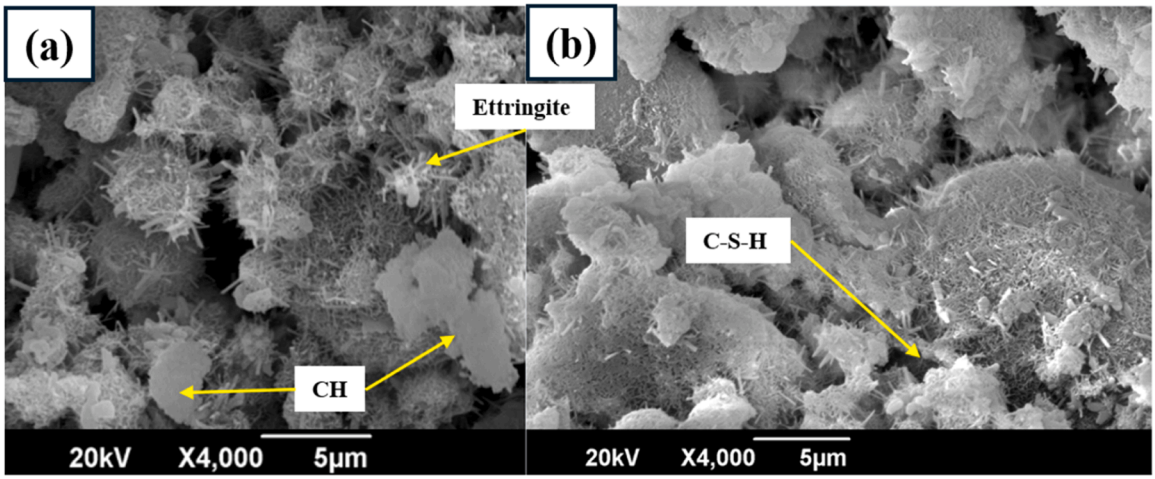

Fig. 15. SEM images of aluminium sulphate-treated sample (AL_ST45), showing ettringite crystal formation.

Table 5
Structural modes of failure.

Sample identification	3D-printed structure	Failure mode	Likely cause of failure
CTRL_ST00 AL_ST15 AL_ST25 AL_ST35	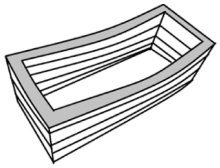	Elastic buckling	▪ Weak layer adhesion. ▪ Homogeneity of mixture. ▪ Insufficient curing time between layers.
AL_ST45	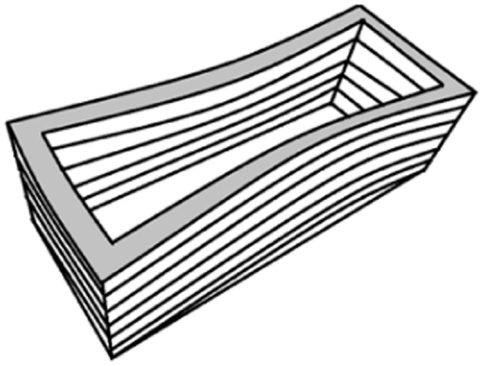	Plastic collapse	▪ Inadequate support / reinforcement. ▪ Lower layers experiencing stresses exceeding yield stress.

A higher slenderness ratio means the structure is slenderer and, therefore, more prone to buckling. As $\frac{l}{t}$ increases, P_{cr} decreases, making it easier for the structure to buckle under a given load. This relationship proves that the height-to0-thickness ratio is a critical factor in determining a structure's stability under vertical loading.

In contrast, sample A5 experienced a more severe failure mode known as plastic collapse. This was characterised by a complete structural failure, where the material had yielded and undergone permanent deformation. The large, irreversible changes in shape, with the material spreading outwards and losing its initial form, indicated that the stress levels had exceeded the yield strength of the concrete. Plastic collapse suggested that the structure could no longer carry any load, leading to a complete loss of structural integrity.

3.4. Effect of printing speed on buildability of 3D-printed small-scale structures

Understanding the critical role of printing speed in 3D printing is essential to optimise the buildability and stability of printed structures. Fig. 16 shows a graphical illustration of the effect of print speed on buildability and extrusion quality. Fig. 17 depicts the results of the investigation, highlighting how varying printing speeds significantly impacted the performance and buildability of small-scale 3D-printed structures. Table 6 presents the effect of printing speed on layer width of the 3D-printed structures.

The investigation into the effect of printing speed on the buildability of 3D-printed small-scale structures revealed distinct differences in performance across different printing speeds. Sample B1, printed at a slow speed of 10 mm/s, resulted in a layer width of 70 mm. This large filament surface area led to several detrimental effects, including excess material being forcefully squeezed onto the printed surface leading to localised buckling of the filament [66], as shown in sample B1 (Fig. 17). Consequently, this resulted in a poor surface finish and nozzle blockage, due to a combination of slow printing speed and constant pump pressure. The excessive material accumulation caused the system to clog after two layers only, making this speed the least effective in terms of buildability. In contrast, sample B2, printed at a speed of 20 mm/s, exhibited optimal buildability with a layer width of 40 mm. This speed enabled the structure to achieve a maximum of 10 layers before structural failure. The layers maintained good adhesion and stability up to the point of collapse, indicating that 20 mm/s was the most effective speed for achieving high buildability. The balanced interaction between material deposition and setting time at this speed ensured strong inter-layer bonding and structural integrity. Sample B3, printed at a higher speed of 40 mm/s and managed to produce 7 layers with a layer width of 20 mm before reaching structural failure. However, the increased speed resulted in early noticeable deformation and reduced layer adhesion when compared to sample B2. The limited settling time for the material at this speed hindered proper layer bonding, reducing the overall buildability and leading to structural failure after fewer layers when compared with sample B2. Finally, sample B4, printed at the highest speed of 80 mm/s, resulted in a layer width of 13 mm. While this speed allowed for the printing of up to five layers, it induced major inconsistencies and weak inter-layer bonding. The rapid deposition rate at this speed influenced the time available for structural build-up between layers. Higher speeds reduced this interval, which limited the material's ability to gain sufficient yield strength before the next layer was deposited. Although the paste's rheological properties remained unchanged, the mechanical timing of deposition interacted with the evolving material stiffness, which affected layer stability. While printing speed did not alter the intrinsic rheological parameters of the material, it influenced how these properties were expressed during the printing process. Therefore, higher speeds increased the shear rate in the

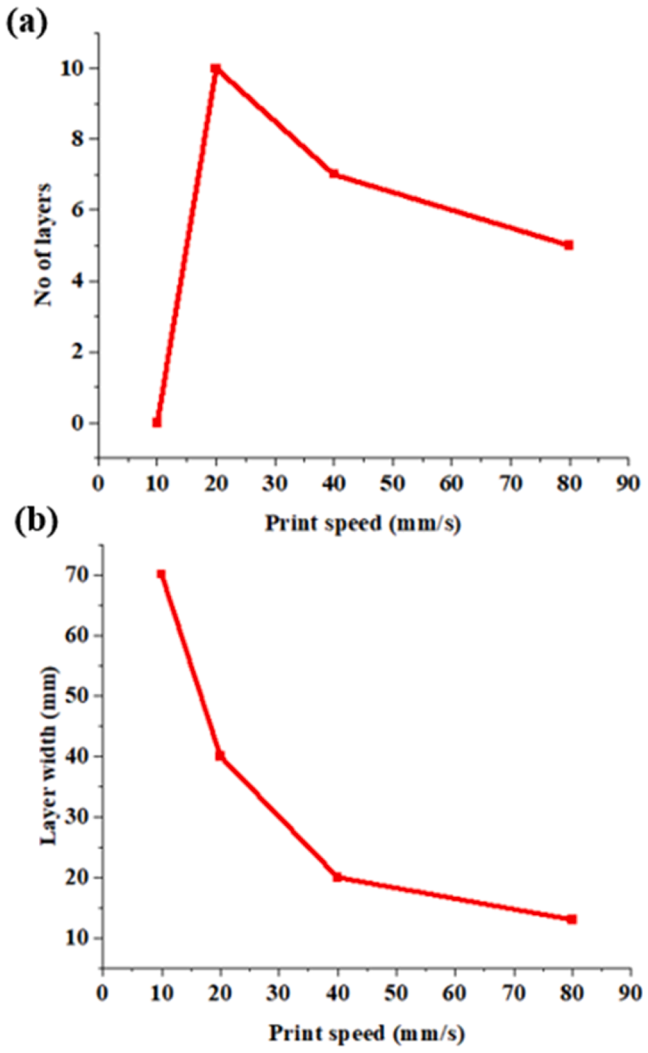

Fig. 16. Graphical illustration of (a) number of layers *versus* printing speeds and (b) layer width *versus* print speed.

Fig. 17. Buildability test with varying printing speeds.

Table 6
Effect of printing speed on layer width of the 3D-printed structures.

Parameters	Samples			
	B1	B2	B3	B4
Printing speed (mm/s)	10	20	40	80
Layer width (mm)	70	40	20	13
No of layers	—	10	7	5

nozzle, temporarily decreased the apparent viscosity due to shear-thinning behaviour, while reducing the time available for thixotropic rebuild between layers. Conversely, lower speeds supported more recovery time, but could lead to excessive deposition and sagging. Therefore, the interaction between printing speed and the fresh-state behaviour of the material directly impacted buildability.

Figs 18 and 19 show the surface contact between 3D-printed layers, the effect of printing speed and pump pressure on the interlayer

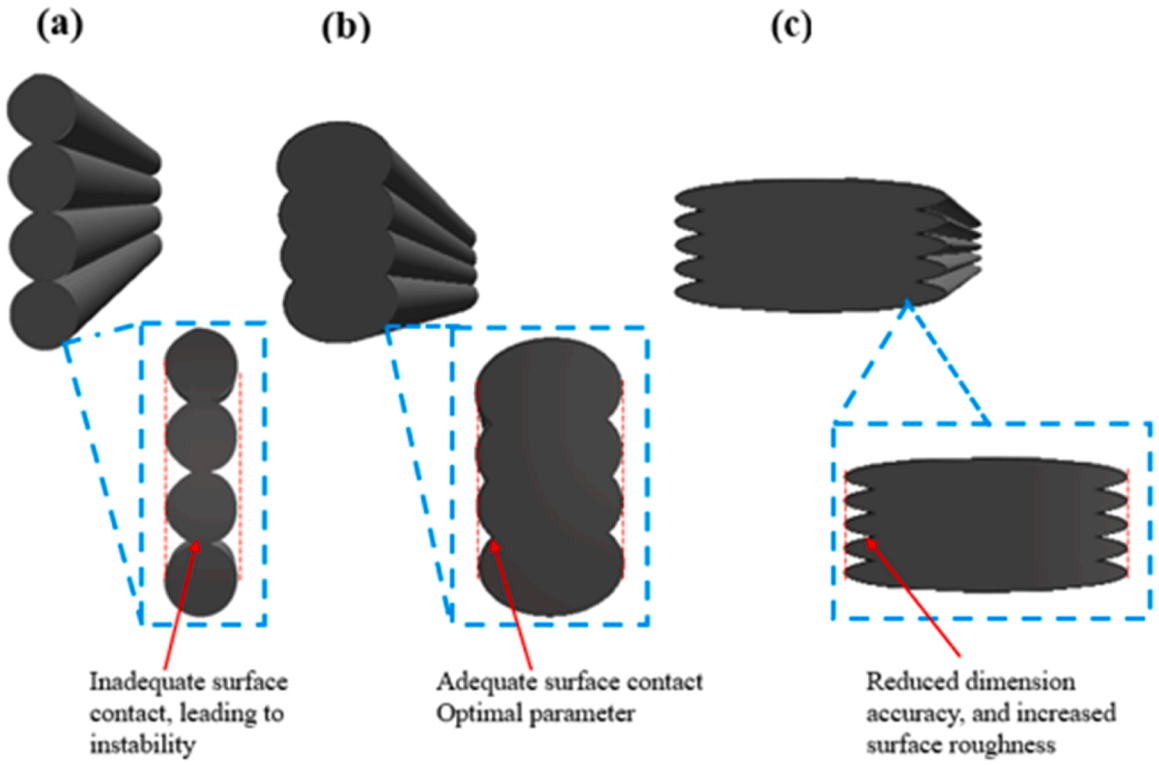

Fig. 18. Surface contact between 3D-printed structures.

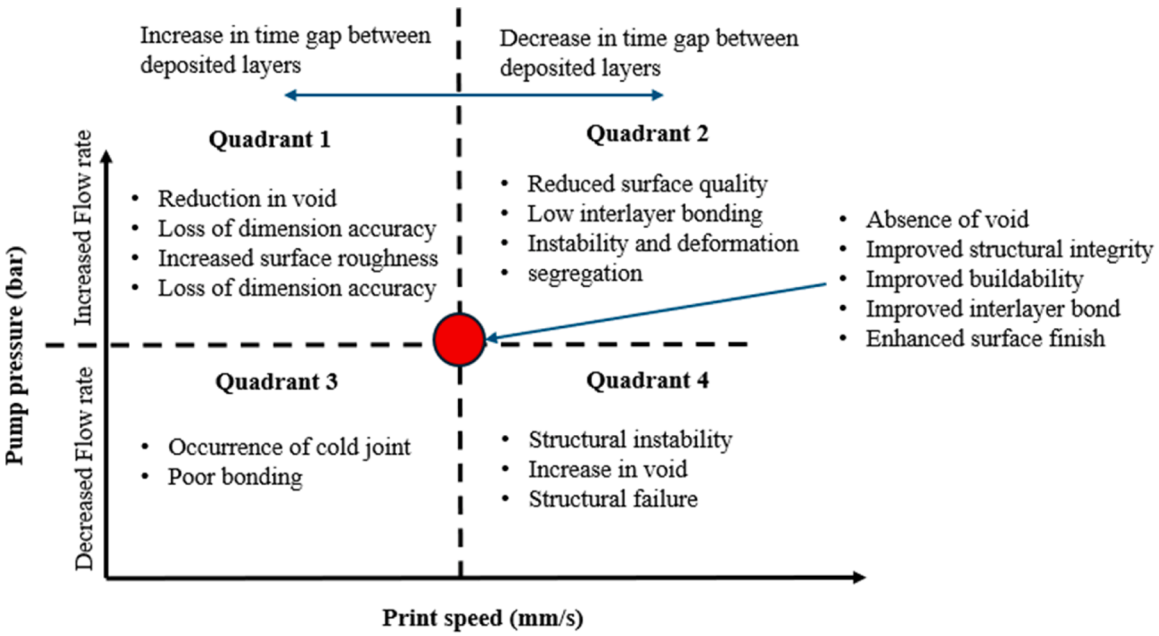

Fig. 19. Printing limits, showing the effects of pump pressure and printing speed on the 3D-printed layers.

bond of 3D-printed structures. The optimal printing speed was identified at the value of 20 mm/s, which allowed for the printing of 14 stable layers with strong inter-layer bonding and stability. Higher speeds, such as 40 and 80 mm/s, resulted in poor layer adhesion and early failure. These findings were consistent with observations reported by Chen et al. [52], who demonstrated that higher shear rates during extrusion could outpace the material's structural recovery, governed by its thixotropic behaviour. This reinforced the

importance of selecting printing speeds that allow sufficient time for material stiffening between layers.

Fig. 19 is divided into 4 quadrants and illustrates how varying print speed, pump pressure, and time gaps between layers affect the build quality and structural stability of 3D-printed concrete. In quadrant 1, a combination of increased pump pressure and decreased print speed results in a reduction of voids but affects the dimensional accuracy and increased surface roughness. This is because the excessive material flow tends to overfill the layers, making it difficult to control the precise placement and leading to poor surface quality. Conversely, quadrant 2, where both pump pressure and print speed are high, shows that the material is deposited too rapidly, reducing surface quality and interlayer bonding. This can cause instability, deformation, and segregation of the material, compromising the structural integrity of the print. Quadrant 3, with low pump pressure and low print speed, results in the occurrence of cold joints and poor bonding between layers. The slow deposition and insufficient material flow create time gaps between layers that prevent proper bonding, leading to weaker connections and potential delamination. On the other hand, in quadrant 4, where low pump pressure is combined with high print speed, risks structural instability and an increase in voids. This imbalance leads to under-extrusion, as the pump is unable to supply enough material to match the high speed of the nozzle, resulting in incomplete layer formation and poor structural strength. At the midpoint, the optimal condition is represented by the red circle, where the pump pressure and print speed are optimised. In this zone, the concrete is deposited evenly, resulting in the absence of voids, improved interlayer bonding, and enhanced surface finish. This central area reflects the ideal operational range for the printing process, where structural integrity and buildability are maximised.

Additionally, Fig. 19 depicts the influence of time gaps between deposited layers, as indicated by the horizontal arrows. Increasing the time gap between layers, as shown by the arrow pointing left, can lead to a loss in dimensional accuracy and rougher surfaces, as the material may not properly bond if the previous layer has already begun to set. Conversely, decreasing the time gap, represented by the arrow pointing right, can reduce surface quality and interlayer bonding, leading to instability and deformation if the layers are deposited too quickly without allowing enough time for each layer to settle.

3.4.1. Analysis of problems using engineering principles and numerical analysis

The relationship between material flow rate, printing speed, and pump pressure are critical in determining the buildability and structural stability of 3D-printed components. These parameters collectively influence material deposition, layer bonding quality, and structural resistance to mechanical stresses like buckling.

3.4.2. Material flow rate and printing speed

The cross-sectional area of the nozzle and the printing speed determine the volumetric flow rate (Q) in 3D printing. The relationship is defined in Eq. (4):

$$Q = A_{nozzle} \times v \tag{4}$$

where Q is the volumetric flow rate (mm^3/s), A_{nozzle} is the cross-sectional area of the nozzle (mm^2), and v is the printing speed (mm/s). Given that the diameter of the nozzle is 15 mm, the cross-sectional area of the nozzle was calculated, using Eq. (5):

$$A_{nozzle} = r^2 \tag{5}$$

$$A_{nozzle} = \frac{\pi \times (15mm)^2}{4} = \frac{3.1416 \quad \times 225}{4} = 176.71 \quad mm^2$$

Using this cross-sectional area, the flow rate for each printing speed used in the experiment can be calculated:
For B1 (speed = 10 mm/s):

$$Q_{B1} = 176.71 \times 10 = 1767.1 mm^3/s$$

Therefore, B2, B3 and B4 = 3534.2, 7068.4 and 14,136.8 mm^3/s, respectively.

At slower speeds (such as, B1 at 10 mm/s), excessive material deposition caused clogging, thicker layers (70 mm), and poor surface finish. Conversely, B4's faster speed (80 mm/s) resulted in thinner layers (13 mm) and weak interlayer bonding, causing the structure to collapse after five layers.

3.4.2.1. Interlayer adhesion and bonding strength. 'Interlayer bonding strength σ_b is a key determinant of the structural stability in 3D printing. It is expressed as Eq. (6):

$$\sigma_b = \alpha.A.\tau \tag{6}$$

where σ_b is the bonding strength (MPa), A is the contact area between layers (mm^2), τ is the bonding time (s), and α is a material-dependent bonding coefficient.

At low printing speeds, such as B1 (10 mm/s), longer bonding times theoretically promote better adhesion. However, excessive material deposition disrupted surface quality, leading to failure after two layers. B2 (20 mm/s) achieved an optimal balance between deposition rate and bonding time, allowing for 10 stable layers. Higher speeds, such as B4 (80 mm/s), reduced bonding time significantly, resulting in weaker adhesion and collapse after five layers.

3.4.2.2. Pump pressure and material deposition. Material flow is also governed by pump pressure and material viscosity. The relationship is given by Eq. (7):

$$Q = \frac{\pi r^4}{8\mu L} \bullet P \tag{7}$$

where r is the nozzle radius (mm), μ is the viscosity of the material (Pa·s), L is the extrusion length (mm) and P is the pump pressure (Pa).

The excessive pump pressure at slower speeds, such as in B1, led to over-extrusion and surface roughness. Conversely, at higher speeds (such as, B4 at 80 mm/s), the pump pressure could not sustain the material flow, causing under-extrusion, thinner layers, and weak interlayer bonding.

3.4.2.3. Buckling and structural stability. Structural stability can be analysed, using Euler's buckling load formula (Eq. (8)):

$$P_{cr} = \frac{\pi^2 EI}{(KL)^2} \tag{8}$$

where, Pcr is the critical buckling load (N), E is the Young's modulus of the material (Pa), I is the second moment of area (mm⁴), K is the column effective length factor (dimensionless), L is the height of the column (mm).

In B1, thicker layers (70 mm) increased the moment of inertia but also the structure's height, decreasing the critical buckling load (P_{cr}) and making it prone to collapse after two layers. For B2 and B3, thinner layers reduced the moment of inertia, mitigating buckling. However, higher speeds like B3 led to poor adhesion, resulting in failure despite avoiding buckling.

3.5. Effect of layer height on 3D-printed small-scale structures

The influence of layer height on the buildability of 3D-printed structures is crucial to optimise the printing quality and structural stability. Therefore, this study further explored how varying layer heights affected the buildability and performance of 3D-printed small-scale structures. Fig. 20 depicts the buildability test with varying layer heights, and Fig. 20 shows the relationship between layer height, layer width (Fig. 21a) and the number of layers required to complete the print (Fig. 21b). Table 7 presents the effect of layer height on layer width of the 3D-printed structures.

The investigation into the effect of layer height on the buildability of 3D-printed small-scale structures revealed distinct differences in performance across different layer heights. These differences can be primarily attributed to the relationship between layer height, interlayer adhesion and structural stability. Sample C1, with a layer height of 10 mm, achieved the highest buildability by printing 10 layers before structural failure. The relatively small layer height of 10 mm facilitated proper interlayer adhesion, contributing to the structural stability of the printed layers. Sample C1 had a layer width of 40 mm, indicating that a smaller layer height allowed for better material adhesion and stronger layer bonding, which in turn enhanced the overall buildability of the structure.

Conversely, sample C2, with a layer height of 15 mm, successfully printed seven layers before experiencing structural failure. While the increase in layer height to 15 mm still allowed for adequate interlayer adhesion, it was less effective when compared with sample C1. Sample C2 exhibited a layer width of 30 mm, which implied that the increase in layer height began to compromise the ability of the material to adhere properly between layers, leading to a reduction in buildability. Sample C3 with a layer width of 28 mm managed to print only four layers before failure occurred. The larger layer height of 20 mm contributed to improper interlayer adhesion, resulting in a reduction in the interlayer bond strength. This is due to the reduced interfacial contact area and increased potential for cold joints, which can lead to weaker structural integrity and increased risk of delamination or cracking.

Finally, sample C4 supported a mere three layers before structural failure occurred. The substantial layer height of 25 mm resulted in a nozzle height far from the previously deposited layer, leading to uncontrolled extrusion (Fig. 22) and significant buildability challenges. This sample exhibited a layer width of 20 mm. The excessive distance between the nozzle and the previously deposited layer resulted in weak interlayer bonding and inadequate structural support, culminating to rapid structural failure. Significantly, the optimal layer height was 10 mm, facilitating proper interlayer adhesion and allowing for the printing of ten layers before structural failure. This observation has been supported by similar studies [5,15] that established that smaller layer heights improved material cohesion and layer bonding, enhancing overall buildability.These result is similar to the creep-induced deformation observed in Chen et al. [51,52], the increase in layer height in this study increased the mechanical load on lower layers, resulting in earlier failure. This reinforces the importance of optimising layer height to minimise deformation under self-weight. Although, layer height did not alter the intrinsic rheological properties of the mix, it modified the mechanical demands on the material during printing. Larger layer heights increased the gravitational load and shear stress on lower layers, requiring faster structural build-up and higher static yield stress to maintain stability. Reduced layer heights imposed lower stresses and allowed more consistent thixotropic recovery between passes, enabling the material to sustain stability throughout the build process.

3.5.1. Analysis of problems using engineering principles and numerical analysis

The buildability and stability of 3D-printed structures depend on the relationship between key factors, such as layer height, adhesion strength, bonding energy, stress distribution and material extrusion. By applying engineering principles and numerical analysis (Eq. (9)), this study examines how these parameters influence the structural integrity of 3D-printed components. The findings

Fig. 20. Buildability test with varying layer heights.

highlight critical design considerations to optimise interlayer bonding, improve stress distribution, and enhance overall build quality.

$$\sigma_{adh} \alpha \frac{A_{\text{int}}}{h} \tag{9}$$

This formula demonstrates that interlayer adhesion strength (σ_{adh}), which represents the force binding two layers, is inversely proportional to the layer height (h) and directly proportional to the interfacial contact area (A_{int}). As the layer height increases, adhesion strength decreases because less material from the new layer adheres to the previous layer.

Sample C1 (layer height of 10 mm): Exhibited the highest buildability, supporting 10 layers before failure. The smaller layer height increased the interfacial contact area, maximising adhesion strength and ensuring structural stability. Sample C4 (layer height of 25 mm): Demonstrated poor buildability, collapsing after only 3 layers. The greater layer height reduced the contact area, weakening adhesion strength and leading to premature failure. This analysis highlights the importance of smaller layer heights for superior interlayer bonding. Increasing layer height compromises buildability by reducing adhesion strength between layers.

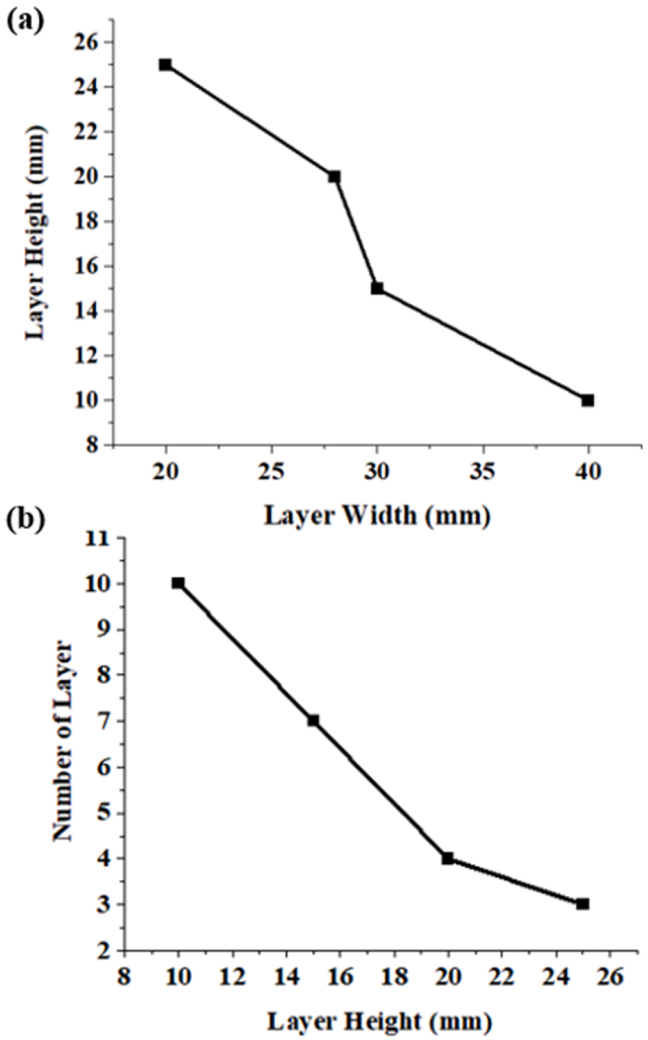

Fig. 21. (a) Effects of layer height on layer width and (b) number of layers required for 3D-printed structures.

3.5.1.1. Stress distribution and structural stability. The distribution of stress within the structure significantly affects buildability. Stress (σ) is calculated in Eq. (10):

$$\sigma = F/A \tag{10}$$

where F is the force (such as the weight of the layers above), and A is the cross-sectional area of each layer. Sample C1, with a smaller layer height, had a larger cross-sectional area A, which distributed the force more evenly across the layers, reducing the overall stress (σ).

Sample C1, with a smaller layer height, the larger cross-sectional area distributed the applied force more evenly, reducing stress levels. This enabled the structure to remain stable and support 10 layers before failure. The larger layer height of sample C4 resulted in a smaller cross-sectional area, concentrating force over a smaller region. This increased stress levels, causing early failure after only 3 layers.

Table 7
Effect of layer height on layer width of the 3D-printed structures.

Parameters		Samples			
		C1	C2	C3	C4
Layer	Layer height (mm)	10	15	20	25
	No of layers	10	7	4	3
	Width (mm)	40	30	28	20

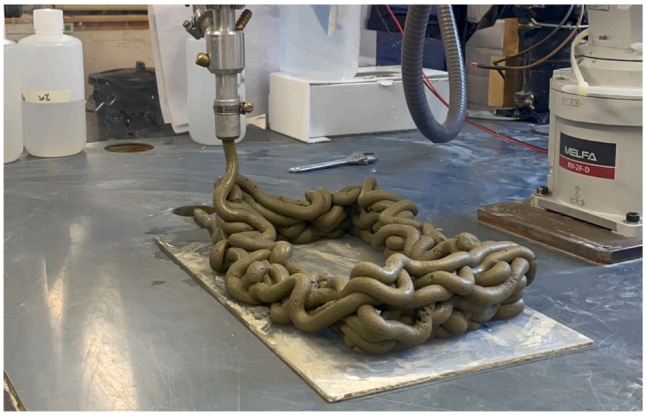

Fig. 22. Uncontrolled nozzle extrusion.

This demonstrates how smaller layer heights promote better stress distribution, enhancing structural stability and buildability.

3.5.1.2. Material extrusion and nozzle height. The quality of material deposition also depends on the volumetric flow rate of the material extruded from the nozzle, described by Eq. (11):

$$Q = \gamma \bullet D \bullet h \tag{11}$$

where Q is the volumetric flow rate, v is the nozzle speed, D is the nozzle diameter, and h is the layer height. Smaller layer heights reduce the required flow rate for uniform deposition, minimising issues such as over-extrusion or under-extrusion. This ensures consistent material layering, enhancing print quality and structural performance.

4. Conclusions

The buildability of cement-based material in a robotic 3D printing setup has been investigated, focusing on the combined effects of printing speed, layer height and aluminium sulphate accelerator dosage. A flowability assessment was also conducted using slump and slump-flow tests to identify the most suitable mortar formulation for extrusion-based printing.

From the results obtained, the following main conclusions can be deduced:

- A mortar mix containing fine sand, SCMs (FA/B = 0.20 and GGBS/B = 0.30), and a W/B ratio of 0.45 demonstrated the highest flowability and was selected for the printing.
- Penetration resistance tests showed no significant setting within 30 min for any mix; however, higher aluminium sulphate dosages exhibited minor early stiffening effects, suggesting enhanced early-age stability under mechanical loading.
- The buildability experiments confirmed that surface misting with a 45% aluminium sulphate solution enabled the successful printing of 14 layers without collapse or deformation, representing the most stable configuration.
- Printing speed significantly affected buildability; a speed of 20 mm/s provided the most stable outcome, while higher speeds led to layer distortion or collapse.
- Layer height also influenced stability; height of 10 mm produced optimal layer adhesion and print quality.
- The study established that the combined tuning of process parameters, material composition, printing speed, layer height and accelerator dosage was crucial for achieving consistent buildability in robotic 3D printing of cement-based materials.

The key contribution of this study includes a structured methodology for evaluating buildability under realistic robotic 3D printing conditions and presents new experimental insights into how aluminium sulphate interacts with print parameters to influence early-age structural stability. These contributions offer a scalable and practical framework for advancing the industrial adoption of 3D-printed cement-based structures.

Finally, this investigation is a part of a two-phase study. Part 1 focused on early-age buildability. Further work, to be presented in Part 2 of this research series, would examine the mechanical performance of the optimised structures, including compressive, flexural, interlayer bond strengths and detailed failure mode analysis, providing a more complete evaluation of the structural viability of 3D-printed cement-based materials.

CRediT authorship contribution statement

Antonios Kanellopoulos: Writing – review & editing, Validation, Supervision, Resources, Project administration, Methodology, Investigation, Formal analysis, Data curation, Conceptualization. **Andreas Chrysanthou:** Writing – review & editing, Validation,

Supervision, Resources, Project administration, Methodology, Investigation, Formal analysis, Data curation, Conceptualization. **Luke Wood:** Writing – review & editing, Validation, Supervision, Software, Resources, Project administration, Methodology, Investigation, Formal analysis, Data curation, Conceptualization. **Oluwatimilehin Disu:** Writing – review & editing, Writing – original draft, Visualization, Validation, Software, Resources, Project administration, Methodology, Investigation, Funding acquisition, Formal analysis, Data curation, Conceptualization. **Sikiru Oluwarotimi Ismail:** Writing – review & editing, Validation, Supervision, Resources, Project administration, Methodology, Investigation, Formal analysis, Data curation, Conceptualization.

Declaration of Competing Interest

The authors declare that there is neither conflict of interest nor funding for this research.

Acknowledgements

The authors, especially the lead author, would like to express their gratitude to the School of Physics, Engineering and Computer Science technical team members for their help and support, especially Alexander Kingstrom, Michael Wilkins, Martin Thomas, Lewis Batt, Emine Dinc and Vienna Unamba, among others.

Data availability

Data will be made available on request.

References

[1] A. Standard, "F2792. 2012 Standard terminology for additive manufacturing technologies, West Conshohocken, PA: ASTM International," See www. astm. org. (doi: 10.1520/F2792-12), 2012.
[2] C.W. Hull, Apparatus for production of three-dimensional objects by stereolithography (No), U. S. Pat. Appl. (1984) 638905.
[3] B. Liu, Y. Chen, D. Li, Y. Wang, S. Geng, K. Qian, "Study on the fracture behavior and anisotropy of 3D-printing PVA fiber-reinforced concrete, Constr. Build. Mater. 447 (2024) 138051.
[4] S.H. Bong, H. Du, Sustainable additive manufacturing of concrete with low-carbon materials, in: A. Ashour, X. Wang, B. Han (Eds.), in Sustainable Concrete Materials and Structures, 11, Woodhead Publishing, 2024, pp. 317–341.
[5] T.T. Le, et al., Hardened properties of high-performance printing concrete, 2012/3//, Cem. Concr. Res. 42 (3) (2012) 558–566, https://doi.org/10.1016/j.cemconres.2011.12.003.
[6] Y.W. Tay, et al., "Processing and properties of construction materials for 3D printing, in: in Materials Science Forum, 861, Trans Tech Publ, 2016, pp. 177–181.
[7] B. Zareiyan, B. Khoshnevis, "Interlayer adhesion and strength of structures in contour crafting - effects of aggregate size, extrusion rate, and layer thickness, 2017/9//, Autom. Constr. 81 (2017) 112–121, https://doi.org/10.1016/j.autcon.2017.06.013.
[8] K.-H. Ler, et al., "Porosity and durability tests on 3D printing concrete: a review, 2024/10/04/, Constr. Build. Mater. 446 (2024) 137973, https://doi.org/10.1016/j.conbuildmat.2024.137973.
[9] Q. Liu, S. Cheng, B. Peng, K. Chen, C. Sun, H. Tang, "The buildability and flexural properties of 3D printed recycled mortar reinforced with synchronized steel cable under different reinforcement ratios, 2024/05/01/, J. Build. Eng. 84 (2024) 108484, https://doi.org/10.1016/j.jobe.2024.108484.
[10] N. Zhang, J. Sanjayan, "Quick nozzle mixing technology for 3D printing foam concrete, 2024/04/15/, J. Build. Eng. 83 (2024) 108445, https://doi.org/10.1016/j.jobe.2024.108445.
[11] Z. Jia, L. Kong, L. Jia, L. Ma, Y. Chen, Y. Zhang, "Printability and mechanical properties of 3D printing ultra-high performance concrete incorporating limestone powder, 2024/05/03/, Constr. Build. Mater. 426 (2024) 136195, https://doi.org/10.1016/j.conbuildmat.2024.136195.
[12] B. Zareiyan, B. Khoshnevis, "Interlayer adhesion and strength of structures in contour Crafting-Effects of aggregate size, extrusion rate, and layer thickness, Autom. Constr. 81 (2017) 112–121.
[13] D. Liu, Z. Zhang, X. Zhang, Z. Chen, "3D printing concrete structures: state of the art, challenges, and opportunities, 2023/11/17/, Constr. Build. Mater. 405 (2023) 133364, https://doi.org/10.1016/j.conbuildmat.2023.133364.
[14] O. Zaid, M.H. El Ouni, "Advancements in 3D printing of cementitious materials: a review of mineral additives, properties, and systematic developments, 2024/05/10/, Constr. Build. Mater. 427 (2024) 136254, https://doi.org/10.1016/j.conbuildmat.2024.136254.
[15] S. Michalopoulos, ""Printable profile of sustainable modified cementitious materials for additive manufacturing applications in digital construction"."
[16] N. Mohamad, K. Muthusamy, R. Embong, A. Kusbiantoro, M.H. Hashim, "Environmental impact of cement production and solutions: a review, Mater. Today. Proc. 48 (2022) 741–746.
[17] L. Masoud, A. Hammoud, Y. Mortada, E. Masad, "Rheological, mechanical, and microscopic properties of polypropylene fiber reinforced-geopolymer concrete for additive manufacturing, 2024/08/09/, Constr. Build. Mater. 438 (2024) 137069, https://doi.org/10.1016/j.conbuildmat.2024.137069.
[18] Y. Lu, J. Xiao, Y. Li, "3D printing recycled concrete incorporating plant fibres: a comprehensive review, 2024/04/26/, Constr. Build. Mater. 425 (2024) 135951, https://doi.org/10.1016/j.conbuildmat.2024.135951.
[19] T. Marchment, J. Sanjayan, M. Xia, "Method of enhancing interlayer bond strength in construction scale 3D printing with mortar by effective bond area amplification, 2019/5//, Mater. Des. 169 (2019), https://doi.org/10.1016/j.matdes.2019.107684.
[20] W. Wu, W. Ye, Z. Wu, P. Geng, Y. Wang, J. Zhao, "Influence of layer thickness, raster angle, deformation temperature and recovery temperature on the shape-memory effect of 3D-printed polylactic acid samples, 2017/8//, Materials 10 (8) (2017), https://doi.org/10.3390/ma10080970.
[21] Z. Liu, M. Li, Y.W.D. Tay, Y. Weng, T.N. Wong, M.J. Tan, "Rotation nozzle and numerical simulation of mass distribution at corners in 3D cementitious material printing, Addit. Manuf. 34 (2020) 101190.
[22] Z. Liu, M. Li, Y. Weng, Y. Qian, T.N. Wong, M.J. Tan, "Modelling and parameter optimization for filament deformation in 3D cementitious material printing using support vector machine, Compos. Part B Eng. 193 (2020) 108018.
[23] R.J.M. Wolfs, F.P. Bos, T.A.M. Salet, "Hardened properties of 3D printed concrete: the influence of process parameters on interlayer adhesion, 2019/5//, Cem. Concr. Res. 119 (2019) 132–140, https://doi.org/10.1016/j.cemconres.2019.02.017.
[24] R.J. Wolfs, F.P. Bos, E.C. Van Strien, T.A. Salet, "A real-time height measurement and feedback system for 3D concrete printing. High Tech Concrete: Where Technology and Engineering Meet: Proceedings of the 2017 fib Symposium, held in Maastricht, The Netherlands, June 12-14, 2017, Springer, 2018, pp. 2474–2483.
[25] S. Gomaa, et al., "3D printing of ultra-high-performance concrete: shape stability for various printing systems, Constr. Build. Mater. 456 (2024) 139039.
[26] G. Ji, J. Xiao, P. Zhi, Y.-C. Wu, N. Han, "Effects of extrusion parameters on properties of 3D printing concrete with coarse aggregates, 2022/03/28/, Constr. Build. Mater. 325 (2022) 126740, https://doi.org/10.1016/j.conbuildmat.2022.126740.

[27] N. Khalil, G. Aouad, K. El Cheikh, S. Rémond, "Use of calcium sulfoaluminate cements for setting control of 3D-printing mortars, Constr. Build. Mater. 157 (2017) 382–391.
[28] Y. Weng, et al., "Printability and fire performance of a developed 3D printable fibre reinforced cementitious composites under elevated temperatures, Virtual Phys. Prototyp. 14 (3) (2019) 284–292.
[29] J. Gardan, L. Hedjazi, A. Attajer, "Additive manufacturing in construction: state of the art and emerging trends in civil engineering, J. Inf. Technol. Constr. (ITcon) 30 (5) (2025) 92–112.
[30] H. Jeong, S.-J. Han, S.-H. Choi, Y.J. Lee, S.T. Yi, K.S. Kim, "Rheological property criteria for buildable 3D printing concrete, Materials 12 (4) (2019) 657.
[31] T.T. Le, S.A. Austin, S. Lim, R.A. Buswell, A.G.F. Gibb, T. Thorpe, "Mix design and fresh properties for high-performance printing concrete, 2012/8//, Mater. Struct. /Mater. Et. Constr. 45 (8) (2012) 1221–1232, https://doi.org/10.1617/s11527-012-9828-z.
[32] B. Panda, S.C. Paul, N.A.N. Mohamed, Y.W.D. Tay, M.J. Tan, "Measurement of tensile bond strength of 3D printed geopolymer mortar, Measurement 113 (2018) 108–116.
[33] J. Kruger, S. Cho, S. Zeranka, C. Viljoen, G. van Zijl, "3D concrete printer parameter optimisation for high rate digital construction avoiding plastic collapse, Compos. Part B Eng. 183 (2020) 107660.
[34] Y.-C. Wu, M. Li, "Effects of Early-Age rheology and printing time interval on late-age fracture characteristics of 3D printed concrete, 2022/10/10/, Constr. Build. Mater. 351 (2022) 128559, https://doi.org/10.1016/j.conbuildmat.2022.128559.
[35] S. Paritala, K.K. Singaram, I. Bathina, M.A. Khan, S.K.R. Jyosyula, "Rheology and pumpability of mix suitable for extrusion-based concrete 3D printing – a review, 2023/10/26/, Constr. Build. Mater. 402 (2023) 132962, https://doi.org/10.1016/j.conbuildmat.2023.132962.
[36] Y. Tao, M.K. Mohan, A.V. Rahul, G. De Schutter, K. Van Tittelboom, "Influence of rheology on mixing homogeneity and mechanical behavior of twin-pipe 3D printable concrete, 2023/12/08/, Constr. Build. Mater. 408 (2023) 133694, https://doi.org/10.1016/j.conbuildmat.2023.133694.
[37] R. Mandal, S.K. Panda, S. Nayak, "Rheology of concrete: critical review, recent advancements, and future prospectives, 2023/08/15/, Constr. Build. Mater. 392 (2023) 132007, https://doi.org/10.1016/j.conbuildmat.2023.132007.
[38] M.T. Souza, I.M. Ferreira, E. n Guzi de Moraes, L. Senff, A.P. Novaes de Oliveira, "3D printed concrete for large-scale buildings: an overview of rheology, printing parameters, chemical admixtures, reinforcements, and economic and environmental prospects,", in: Journal of Building Engineering, 32, Elsevier Ltd, 2020.
[39] C. Joh, J. Lee, T.Q. Bui, J. Park, I.-H. Yang, "Buildability and mechanical properties of 3D printed concrete, Materials 13 (21) (2020) 4919.
[40] G. Ma, Z. Li, L. Wang, "Printable properties of cementitious material containing copper tailings for extrusion based 3D printing, Constr. Build. Mater. 162 (2018) 613–627.
[41] Y. Zhang, Y. Zhang, G. Liu, Y. Yang, M. Wu, B. Pang, "Fresh properties of a novel 3D printing concrete ink, 2018/6//, Constr. Build. Mater. 174 (2018) 263–271, https://doi.org/10.1016/j.conbuildmat.2018.04.115.
[42] S.C. Paul, Y.W.D. Tay, B. Panda, M.J. Tan, "Fresh and hardened properties of 3D printable cementitious materials for building and construction, Arch. Civ. Mech. Eng. 18 (2018) 311–319.
[43] S. Bhattacherjee, M. Santhanam, "Enhancing Buildability of 3D Printable Concrete by Spraying of Accelerating Admixture on Surface, in: in RILEM Bookseries, 28, Springer, 2020, pp. 13–22.
[44] D. Han, R.D. Ferron, "Effect of mixing method on microstructure and rheology of cement paste, Constr. Build. Mater. 93 (2015) 278–288.
[45] F.-J. Rubio-Hernández, "Rheological behavior of fresh cement pastes, Fluids 3 (4) (2018) 106.
[46] M.A.H. Khan, et al., "Comprehensive review of 3D printed concrete, life cycle assessment, AI and ML models: materials, engineered properties and techniques for additive manufacturing, 2025/04/01/, Sustain. Mater. Technol. 43 (2025) e01164, https://doi.org/10.1016/j.susmat.2024.e01164.
[47] V.N. Nerella, M.A.B. Beigh, S. Fataei, V. Mechtcherine, "Strain-based approach for measuring structural build-up of cement pastes in the context of digital construction, Cem. Concr. Res. 115 (2019) 530–544.
[48] S. Kim, T. Kim, B. Kim, H.-d Kim, J. Kim, H. Lee, "Early hydration and hardening of OPC-CSA blends for cementitious structure of 3D printing, Adv. Appl. Ceram. 119 (7) (2020) 393–397.
[49] S.M.V. Anand and S.K. Agarwala, Concrete Technology: Theory and Practice. India, 2023.
[50] M. Tramontin Souza, et al., "Role of chemical admixtures on 3D printed portland cement: assessing rheology and buildability, 2022/1//, Constr. Build. Mater. 314 (2022), https://doi.org/10.1016/j.conbuildmat.2021.125666.
[51] M. Chen, et al., "Rheological parameters, thixotropy and creep of 3D-printed calcium sulfoaluminate cement composites modified by bentonite, 2020/04/01/, Compos. Part B Eng. 186 (2020) 107821, https://doi.org/10.1016/j.compositesb.2020.107821.
[52] M. Chen, et al., "Use of creep and recovery protocol to assess the printability of fibre-reinforced 3D printed White portland cement composites, 2024/12/31, Virtual Phys. Prototyp. 19 (1) (2024) e2331201, https://doi.org/10.1080/17452759.2024.2331201.
[53] S. Bhattacherjee, M. Santhanam, "Investigation on the effect of alkali-free aluminium sulfate based accelerator on the fresh properties of 3D printable concrete, Cem. Concr. Compos. 130 (2022) 104521.
[54] Cemex, "Experts in mortar", available at ⟨https://www.cemex.co.uk/experts-in-mortar⟩, (Accessed on 20th April 2024).
[55] Conserv, "Lime mortar, lime plaster and lime render", available at ⟨https://www.lime-mortars.co.uk/⟩ (Accessed on 20th April 2024).
[56] M. Calì, "Stress Concentration Factors in loaded strips and bars," A thesis of Bachelor degree submitted to Institut Superieur de l'Aeronautique et de l'Espace (ISAE-SUPAERO), Università Degli Studi Di Napoli Federico Ii Scuola Politecnica E Delle Scienze Di Base, 2020.
[57] Z. Li, et al., "Fresh and hardened properties of extrusion-based 3D-printed cementitious materials: a review, in: Sustainability, 12, MDPI AG, *Switzerland*, 2020.
[58] A.R. Krishnaraja, K.V. Guru, "3D printing concrete: a review, 2021/2//, IOP Conf. Ser. Mater. Sci. Eng. 1055 (1) (2021) 012033, https://doi.org/10.1088/1757-899x/1055/1/012033.
[59] Z. Li, et al., "Fresh and hardened properties of extrusion-based 3D-printed cementitious materials: a review, in: Sustainability, 12, MDPI AG, Switzerland, 2020.
[60] A. Das, Y. Song, S. Mantellato, T. Wangler, D.A. Lange, R.J. Flatt, "Effect of processing on the air void system of 3D printed concrete, 2022/06/01/, Cem. Concr. Res. 156 (2022) 106789, https://doi.org/10.1016/j.cemconres.2022.106789.
[61] M. Papachristoforou, V. Mitsopoulos, M. Stefanidou, "Evaluation of workability parameters in 3D printing concrete, 2018/01/01/, Procedia Struct. Integr. 10 (2018) 155–162, https://doi.org/10.1016/j.prostr.2018.09.023.
[62] Y.W.D. Tay, Y. Qian, M.J. Tan, "Printability region for 3D concrete printing using slump and slump flow test, 2019/10/01/, Compos. Part B Eng. 174 (2019) 106968, https://doi.org/10.1016/j.compositesb.2019.106968.
[63] C. Kan, M. Lan, L. Kong, J. Yang, "Effect of aluminium sulfate on cement properties, in: Materials Science Forum, 743-744, Trans Tech Publications Ltd, 2013, pp. 285–291, https://doi.org/10.4028/www.scientific.net/MSF.743-744.285.
[64] I. Dressler, N. Freund, D. Lowke, "The effect of accelerator dosage on fresh concrete properties and on interlayer strength in shotcrete 3D printing, 2020/1//, Materials 13 (2) (2020), https://doi.org/10.3390/ma13020374.
[65] A.S.J. Suiker, R.J.M. Wolfs, S.M. Lucas, T.A.M. Salet, "Elastic buckling and plastic collapse during 3D concrete printing, 2020/09/01/, Cem. Concr. Res. 135 (2020) 106016, https://doi.org/10.1016/j.cemconres.2020.106016.
[66] W. Lao, M. Li, T.N. Wong, M.J. Tan, T. Tjahjowidodo, "Improving surface finish quality in extrusion-based 3D concrete printing using machine learning-based extrudate geometry control, Virtual Phys. Prototyp. 15 (2) (2020) 178–193.